Temperature uniformity in the CERN CLOUD chamber

António Dias[1], Sebastian Ehrhart[1,2], Alexander Vogel[1], Christina Williamson[3,4], João Almeida[1,5], Jasper Kirkby[1,5], Serge Mathot[1], Samuel Mumford[1], and Antti Onnela[1]

[1]CERN, CH-1211 Geneva, Switzerland
[2]Max Planck Institute for Chemistry Atmospheric Chemistry Department Hahn-Meitner-Weg 1, 55128 Mainz, Germany
[3]CIRES, University of Colorado, Boulder, CO
[4]Chemical Sciences Division, NOAA Earth System Research Laboratory, Boulder, CO
[5]Goethe University Frankfurt, Institute for Atmospheric and Environmental Sciences, 60438 Frankfurt am Main, Germany

Correspondence to: António Dias (amcbd89@gmail.com)

Abstract. The CLOUD (Cosmics Leaving OUtdoor Droplets) experiment at CERN is studying the nucleation and growth of aerosol particles under atmospheric conditions, and their activation into cloud droplets. A key feature of the CLOUD experiment is precise control of the experimental parameters. Temperature uniformity and stability in the chamber are important since many of the

5 processes under study are sensitive to temperature and also to contaminants that can be released from the stainless steel walls by upward temperature fluctuations. The air enclosed within the 3 m CLOUD chamber is equipped with several arrays ("strings") of high precision, fast-response thermometers to measure its temperature. Here we present a study of the air temperature uniformity inside the CLOUD chamber under various experimental conditions. Measurements were performed

10 under calibration conditions and run conditions, which are distinguished by the flow rate of fresh air and trace gases entering the chamber: 20 l/min and up to 210 l/min, respectively. During steady-state calibration runs between -70°C and +20°C, the air temperature uniformity is better than ±0.06°C in the radial direction and ±0.1°C in the vertical direction. Larger non-uniformities are present during experimental runs, depending on the temperature control of the make-up air and trace gases (since

15 some trace gases require elevated temperatures until injection into the chamber). The temperature stability is a few times 0.01°C over periods of several hours during either calibration or steady-state run conditions. During rapid adiabatic expansions to activate cloud droplets and ice particles, the chamber walls are up to 10°C warmer than the enclosed air. This results in larger non-uniformities while the air returns to its equilibrium temperature with time constant of about 200 s.

1   Introduction

The Intergovernmental Panel on Climate Change (IPCC) considers that the largest source of uncertainty in anthropogenic radiative forcing of the climate is due to increased aerosol since pre-industrial times, and its effect on clouds (Myhre et al., 2013). Most of the increased aerosol has resulted from anthropogenic precursor vapours that, after oxidation in the atmosphere, form particles which may
25 grow to become new cloud condensation nuclei (CCN). By current estimates, about half of all CCN originate from nucleation rather than being emitted directly into the atmosphere (Merikanto et al., 2009), but the vapours and mechanisms responsible remain relatively poorly known.

The CLOUD experiment at CERN (Kirkby et al., 2011; Duplissy et al., 2016) has achieved sufficient suppression of contaminants inside a large, 3 m diameter stainless steel chamber to allow con-
30 trolled aerosol nucleation, growth and activation experiments to be performed in the laboratory under atmospheric conditions. The chamber is filled with humidified artificial air to which is added ozone and selected trace vapours. Several adjustable ultra violet (UV) light sources illuminate the contents of the chamber via fibre optic and other systems to simulate atmospheric photolytic chemistry. The ion concentrations inside the chamber can be precisely controlled over the full tropospheric range
35 with a pion beam from the CERN Proton Synchrotron. Moreover, an ion-free environment can be created with a pair of high voltage electrodes set to ± 30 kV, which sweep all ions from the chamber in less than 1 s. The chamber is equipped with a comprehensive array of state-of-the-art instruments that continuously samples and analyses its contents, including mass spectrometers to measure the molecular composition of the nucleating clusters and rule out any influence from contaminants. To
40 ensure adequate mixing of the 27 m^3 stainless steel chamber, two large mixing fans operate on the top and bottom of the chamber(Voigtlander et al., 2012)

The CLOUD chamber normally operates at 5 mbar above atmospheric pressure (the small excess ensures no contaminant vapour enter the chamber through the sampling ports). However, the chamber can also be operated in a classical Wilson cloud chamber mode to create liquid or ice clouds.
45 During this operation, air in the chamber at high relative humidity (>90% RH) is first raised to 220 mbar above atmospheric pressure and then allowed to reach thermal equilibrium. When equilibrium is reached, the pressure in the chamber exhaust pipe is reduced to 65 mbar below atmospheric with a high-volume blower, and then the main air inlet valve for the chamber is closed. A controlled adiabatic pressure reduction is then performed back down to 5 mbar overpressure, which cools the
50 air and forms a liquid or ice cloud when the RH in the chamber rises above 100%. The pressure reduction is controlled with two regulation valves and two gate valves, which provide a selectable and highly flexible pressure profile lasting between 10 s and 10 minutes. The low exhaust pressure (-65 mbar) ensures sufficient pressure difference to drive the expansion down to a final 5 mbar chamber overpressure. Once the chamber reaches 5 mbar, the main air valve is re-opened to maintain that
55 pressure. During the expansion a cloud is maintained in the chamber and experiments are performed on cloud processing of aerosols, ice nucleation, and the effects of charge on cloud microphysics.

The cycle can be repeated up to three or more times with a single CCN population, so the effects of multiple cloud processing of aerosol can be studied.

2 CLOUD thermal system

As well as precise control of trace precursor vapours, UV intensity, ions, relative humidity and pressure, it is important to maintain good temperature uniformity and stability in the CLOUD chamber since many of the processes under study are sensitive to temperature, and contaminants can be released from the walls by positive temperature fluctuations (Duplissy et al., 2010). Here we present a study of the air temperature uniformity inside the CLOUD chamber during a calibration campaign, late July 2014, and the CLOUD9 data campaign, September–November 2014. In addition, we calibrated the Pt100 calibration strings (PTH and PTV, see below) in the laboratory during early July 2014. Concerning the present paper, the two CLOUD campaigns are distinguished by the flow rate of fresh air and trace gases entering the chamber: 10 l/min and 210 l/min, respectively. The high flow rate during the data campaign is required to compensate for the sampling flows of analysing instruments attached to the chamber. During both campaigns the main air supply passes through a 10 m "serpentine" pipe inside the CLOUD thermal housing (see below) to bring its temperature close to that of the chamber air before injection. However, during measurement campaigns, some trace gases are injected warm into the chamber at flow rates of around 1 l/min each, which can influence the temperature uniformity inside the chamber.

The CLOUD chamber is enclosed in a thermal housing designed to maintain a highly uniform and stable air temperature inside the chamber at any value between -70°C and +100°C. Experiments are performed at temperatures below 30°C; cleaning of the chamber walls by bakeout of contaminants is performed at 100°C(Kirkby et al., 2011; Duplissy et al., 2016; Kupc et al., 2011). Figure 1 shows a schematic of the CLOUD thermal system and its components.

The temperature of the air inside the CLOUD chamber is measured by several precision thermometer strings: a) three horizontal strings oriented radially near the mid plane of the chamber that use either platinum resistance thermometers (Pt100, denoted PT and PTH) or thermocouples (TC) and b) two vertical strings that use either GaAs optical sensors (OS) or Pt100 sensors (PTV). The Pt100 sensors are four-wire sensors with National Instruments (National Instruments Corp.) NI 9217 readout electronics. The Pt100 calibration strings, PTH and PTV, are only installed during calibration campaigns, when no electric field is present. Figure 2 shows some details of the TC and OS strings. The thermocouple sensors are type K with National Instruments (National Instruments Corp.) NI 9214 readout electronics. GaAs optical sensors (OTG-F with Pico-M single channel readout; Opsens Inc.) are used for the vertical temperature string since the high electrical field rules out the use of conventional thermometer sensors with electrical wires. The thermocouple and optical sensors have a low mass (0.5 mm diameter sensor tip with 75 μm stainless steel wall thickness and

30 mm free length) and a fast response time: 3 s ($1/e$) in air. However the Pt100 sensors have a higher mass (1.5 mm diameter stainless steel sheath with 100 μm wall thickness) and slower response time (180 s in air). The positions of the temperature sensors of all five strings (TC/PTH, OS/PTV and PT) in the CLOUD chamber are summarised in Table 1.

3 Temperature uniformity during calibration and nucleation experiments

The thermal non-uniformities over the large volume of the CLOUD chamber are small and require precise ($\sim$0.01°C) calibration of the temperature sensors. We therefore constructed dedicated horizontal and vertical Pt100 calibration strings (PTH and PTV, respectively) in which each sensor had been calibrated in close proximity to a certified WIKA (WIKA Alexander Wiegand SE & Co. KG) Pt100 reference thermometer, which itself was calibrated to to 0.03°C absolute precision. The PTH and PTV strings were then mounted in the CLOUD chamber alongside the TC and OS strings, respectively, to transfer the calibrations. The calibration procedure is described in detail in Appendix A. All the measurements presented in the following analysis correspond to calibrated sensor temperatures.

Figure 3 shows some typical examples of the time series of thermometer sensors during experimental runs and calibration periods. When the experimental conditions are not adjusted, the temperatures of individual sensors show drifts of only a few 0.01°C over periods of several hours. Figure 4 shows the temperature residuals of individual sensors from their mean values, after slow trends in the data have been removed. The standard deviations of Gaussian fits to the data are 0.012°C, 0.018°C, and 0.004°C for the TC, OS and PT strings, respectively. Comparison of the TC and PT residuals shows that short term (>15 s) fluctuations of the air temperature in the CLOUD chamber are very small (<0.01°C). Furthermore, the comparably small OS residuals show that these sensors are in principle capable of around 0.01°C measurement precision.

Figure 5 shows representative temperature non-uniformities measured by several sensor strings in the radial and vertical directions during calibration runs at 21°C and 1°C, respectively. For these data, the temperature non-uniformity (maximum difference from the mean for the entire string) measured by the Pt100 calibration strings is ±0.01°C in the radial direction and ±0.04°C in the vertical direction. Comparison with the other strings shows close agreement of the TC string (panel a) but somewhat larger residuals for the OS string (panel b), reflecting larger systematic errors in the OS calibration.

Figure 6 shows the temperature non-uniformity in the horizontal and vertical directions at chamber temperatures between -70°C and 20°C. The temperature non-uniformity is characterised as the maximum temperature difference of any sensor from the string mean, Max ΔT. A clear trend is seen in all temperature strings for increasing non-uniformity as the chamber temperatures is lowered, which results from an increased difference with the experimental hall temperature (around 20°C). Never-

theless, under ideal (calibration) conditions the temperature uniformity is better than ±0.06°C in the radial direction and ±0.1°C in the vertical direction, for chamber temperatures between -70°C and +20°C. During data taking, there is a high flow flow of fresh make-up air and trace gases (210 l/min) which can lead to higher non-uniformities in the vertical direction of up to ±0.5°C (green triangle symbols in panel b), depending on the temperature control of the make-up air. However, even during data taking, the radial temperature uniformity remains better than ±0.06°C.

4   Temperature characteristics during cloud formation experiments

Following an adiabatic pressure reduction, the temperature of the air in the chamber is below that of the walls. The wall temperature is essentially unaffected by the adiabatic cooling since its mass is several hundred times greater than the enclosed air mass. Therefore the walls transfer heat into the air and eventually bring it back into equilibrium at its original temperature, before the pressure reduction took place. The rate of warming of the air can be described by a Newton's cooling law (Incropera and DeWitt, 2007):

$$\frac{\partial T}{\partial t} = -\frac{A\mu}{C}T = -\lambda T,$$

where A is the area of the chamber, μ is the heat transfer coefficient between the walls and the air, and C is the heat capacity of the air. These constants are absorbed into a single reheating rate, λ, that characterises the CLOUD chamber. The characteristic reheating rate can be obtained by fitting the temperature versus time with an exponential curve given by

$$T(t) = T_w + (T_0 - T_w)e^{-\lambda t}, \tag{1}$$

where T_w is the wall temperature and T_0 is the initial temperature at $t = 0$, immediately after the adiabatic pressure reduction has finished. The characteristic reheating time constant, $\tau = 1/\lambda$.

Around 300 adiabatic expansion (pressure reduction) experiments were performed during CLOUD9, September–November 2014. All were analysed and combined to improve the statistical precision of the results. Figure 7 shows an example of an adiabatic expansion to form a cloud in the CLOUD chamber. The pressure reduction takes place over a period of 5 minutes, after which the temperature returns to its equilibrium value over the next 30 minutes. The red line shows an exponential fit to the reheating period (Eq. 1) with a time constant, $\tau = 200$ s. Figure 8 shows that the characteristic reheating rate is the same everywhere in the chamber. This is expected for a well-mixed chamber. Figure 9 shows that λ is only weakly dependent on the initial temperature reduction, ΔT. The slight dependence on ΔT probably results from the increased importance of relatively warm make-up air at high ΔT.

During adiabatic expansions, air temperatures are up to 10°C cooler than the walls, so large thermal non-uniformities may be anticipated. In Fig. 10 we show an example of the temperatures measured with vertical and horizontal strings during and after a fast (80 seconds) adiabatic pressure

reduction at -30°C. Compared with operation under equilibrium conditions (Fig. 6), much larger non-uniformities of up to around ±1.0°C are present at the minimum temperature after an adiabatic expansion, in both radial and vertical directions (turbulence during an expansion ensures complete mixing of the chamber). Thermal non-uniformities in the radial direction subsequently decrease as

165 the air reheats. However, non-uniformities in the vertical direction reach a maximum around 2 minutes after the end of the expansion. The vertical string shows clear evidence of thermal stratification as the chamber reheats, with warmer air flowing to the upper part in the chamber (Fig. 6c). The radial string shows the effect of relatively warm make-up air entering the chamber after the expansion has finished and the main air inlet valve has been re-opened to maintain the baseline chamber pressure at

170 +5 mbar. This can be seen in Fig. 6d by the higher temperatures of TC5 and TC6, which are closest to the axis of the chamber and mixing fans. The flow of relatively warm make-up air partly contributes to the vertical stratification since the air exhaust pipes are located at the top of the chamber.

5   Conclusions

In order to characterise the temperature uniformity of the air inside the CERN CLOUD chamber,
175 we have constructed and calibrated several thermometer strings using various sensors (Pt100, thermocouple and optical/GaAs). Our measurements show that, under stable calibration conditions, the temperature uniformity is better than ±0.06°C in the radial direction and ±0.1°C in the vertical direction, for chamber temperatures between -70°C and +20°C. This excellent performance for a large-volume (26.1 m^3) chamber underscores the quality of the CLOUD thermal control system and

180 thermal housing. Moreover, during periods when the experimental conditions are not adjusted, the chamber air drifts only a few 0.01°C. During data taking, there is a high flow flow of fresh make-up air and trace gases—up to around 200 l/min—to compensate for the air extracted into sampling instruments. This can lead to higher thermal non-uniformities unless the make-up air is carefully adjusted to match the chamber temperature before injection. Larger non-uniformities of up to around

185 ±1.0°C occur during adiabatic expansions to form clouds in the chamber, since the walls are up to 10°C warmer than the enclosed air. After an adiabatic expansion, the chamber air is reheated by the walls and returns to its equilibrium temperature with a time constant of around 200 s.

Appendix A: Thermometer sensor calibrations

Calibration of the horizontal and vertical Pt100 calibration strings

190 Careful calibration of all thermometer sensors used in the CLOUD chamber is required to extract meaningful results from the thermal measurements. Calibration of the sensors in the horizontal and vertical Pt100 calibration strings (PTH and PTV, respectively) was carried in the laboratory in early July 2014. After calibration and assembly of the PTH and PTV strings, they were mounted in the

chamber alongside the TC and OS strings, respectively, and then used to calibrate the latter two
strings *in situ*, as described below.

The Pt100 calibration strings are designed to allow the sensors to be dismounted without disconnecting from their readout electronics (Fig. A1). In this way the Pt100 sensors can be placed in close proximity during inter-calibration in water baths or liquid nitrogen, and the calibrations cannot be affected by disconnecting and reconnecting readout electronics. A certified WIKA (WIKA Alexander Wiegand SE & Co. KG) Pt100 reference thermometer–calibrated according to ISO standard IEC751—was used as the absolute reference to calibrate the individual PTH and PTV sensors. The WIKA Pt100 reference thermometer is calibrated to 0.03°C absolute systematic temperature uncertainty in the range 0–100°C.

The PTH and PTV sensors were calibrated according to the Calendar-Van Dusen (CVD) equationCallendar (1887); Dusen (1925), which relates the resistance, R (Ω) and temperature, T (°C) of platinum resistance thermometers by:

$$R(T) = \begin{cases} R_0 \left[1 + A\,T + B\,T^2 \right] & \text{if } T \geq 0 \\ R_0 \left[1 + A\,T + B\,T^2 + (T-100)\,C\,T^3 \right] & \text{if } T < 0 \end{cases} \tag{A1}$$

The standard values for a Pt100 sensor are as follows: $R_0 = 100\ \Omega$, $A = 3.908 \times 10^{-3}\ \Omega\ °C^{-1}$, $B = -5.775 \times 10^{-7}\ \Omega\ °C^{-2}$ and $C = -4.183 \times 10^{-12}\ \Omega\ °C^{-3}$ Commission et al. (2008). We determined fitted values of these parameters for each of our Pt100 sensors in our calibration procedure, as described below.

All calibration string Pt100 sensors were wired through their respective strings and connected to their readout electronics. The sensors were then placed in close proximity in a liquid bath along with the reference Pt100 thermometer. Care was taken to ensure that no sensors were in direct physical contact. The Huber CC-K15 liquid bath (Huber Kältemaschinenbau AG) controlled the water temperature to better than 0.02°C stability over the calibration range from 2°C to 70°C. For calibration at lower temperatures, the sensors and reference Pt100 were placed in a dewar filled with liquid nitrogen. The temperature measured at the boiling point of liquid nitrogen agreed within 0.01 ºC with standard value for nitrogen at the measured atmospheric pressure (-196.21 º C at 966 mbar).

A least squares fit of Eq. A1 was then applied to the calibrated temperature measurements for each Pt100 sensor. The C parameter was fixed at the standard value since it was poorly constrained by the calibration points. Moreover, propagation of the uncertainties showed that uncertainties in B have a larger effect than uncertainties in C. The residuals of the fit are shown in Fig. A2, and the fitted parameters and errors and uncertainties are summarised in Table A1.

A Monte Carlo method was performed to evaluate the temperature uncertainties of the Pt100 sensors corresponding to their fitted CVD parameters. A sample of 1000 of fit parameters were chosen for each sensor at a given temperature from their respective values and errors, and the resistances were calculated. The resistances were then converted into temperatures. The standard deviation of these temperature distributions were then taken to be the measurement error at that temperature.

230 This was repeated at various temperatures over the range from -70°C to +70°C. The results are summarised in Fig. A3 and show that almost all Pt100 calibration sensors have an uncertainty below 0.01°C over the full temperature range.

Calibration of the thermocouple, optical sensor and horizontal PT100 string

After calibrating the Pt100 calibration sensors, they were mounted in their respective strings and
235 placed inside the CLOUD chamber for the calibration campaign. In this way, each TC and OS sensor now had a calibrated Pt100 sensor in close proximity that was used to define the calibrated temperature at that location. In the case of the PT string, a linear interpolation was assumed to derive the calibrated temperatures at the positions of its sensors.

To calibrate the TC and OS sensors, the difference between the temperature measured by each
240 sensor (T_s) and it's adjacent calibrated Pt100 sensor (T^*) was fitted to a polynomial:

$$T^* - T_s = \sum_{n=0}^{k_s} x_n T_s^n, \tag{A2}$$

where x_n are fitted coefficients and k_s is the degree of the polynomial fit required for each sensor. The fitted parameters are then subsequently used to correct each measured sensor temperature to its calibrated value.

245 A least squares fit of Eq. A2 was applied to the calibrated temperature measurements for each TC sensor. A second order fit was found to best describe the data (Fig. A4a). The TC fit residuals are shown in Fig. A4b. We summarise the fitted calibration parameters and uncertainties for the thermocouple string in Table A2.

The optical sensors were calibrated in a similar way. Here a 3rd order polynomial was used, except
250 for OS4 and OS5, which required a 4th order polynomial (Fig. A5a). OS4 displayed anomalous behaviour (and, to a lesser extent, also OS5) and so both were eliminated from analyses of the temperature uniformity in the CLOUD chamber. The OS fit residuals are shown in Fig. A5b and are somewhat larger than those obtained for the TC sensors. We summarise the fitted calibration parameters and uncertainties for the optical sensor string in Table A3.

255 The PT sensors were calibrated using a least squares fit to a linear function of the measured temperature (T_{PT}):

$$T(T_{PT}) = x_1 T_{PT} + x_0 \tag{A3}$$

The results of these fits are summarised in Table A4.

Acknowledgements. This research has been supported by a Marie Curie Initial Training Network Fellowship of
260 the European Community's Seventh Framework Programme under contract number (PITN-GA-2012-316662-CLOUD-TRAIN.)

References

Callendar, H. L.: On the Practical Measurement of Temperature: Experiments Made at the Cavendish Laboratory, Combridge, Philosophical Transactions of the Royal Society A: Mathematical, Physical and Engineering Sciences, 178, 161–230, doi:10.1098/rsta.1887.0006, https://doi.org/10.1098%2Frsta.1887.0006, 1887.

Commission, I. E. et al.: IEC 60751: 2008, Industrial platinum resistance thermometers and platinum temperature sensors, 2008.

Duplissy, J., Merikanto, J., Franchin, A., Tsagkogeorgas, G., Kangasluoma, J., Wimmer, D., Vuollekoski, H., Schobesberger, S., Lehtipalo, K., Flagan, R. C., Brus, D., Donahue, N. M., Vehkamaki, H., Almeida, J., Amorim, A., Barmet, P., Bianchi, F., Breitenlechner, M., Dunne, E. M., Guida, R., Henschel, H., Junninen, H., Kirkby, J., Kurten, A., Kupc, A., Maattanen, A., Makhmutov, V., Mathot, S., Nieminen, T., Onnela, A., Praplan, A. P., Riccobono, F., Rondo, L., Steiner, G., Tome, A., Walther, H., Baltensperger, U., Carslaw, K. S., Dommen, J., Hansel, A., Petaja, T., Sipila, M., Stratmann, F., Vrtala, A., Wagner, P. E., Worsnop, D. R., Curtius, J., and Kulmala, M.: Effect of ions on sulfuric acid-water binary particle formation: 2. Experimental data and comparison with QC-normalized classical nucleation theory, Journal of Geophysical Research: Atmospheres, 121, 1752–1775, doi:10.1002/2015JD023539, http://dx.doi.org/10.1002/2015JD023539, 2015JD023539, 2016.

Duplissy, J. et al.: Results from the CERN pilot CLOUD experiment, Atm. Chem. Phys., 10, 1635–1647, 2010.

Dusen, M. S. V.: PLATINUM-RESISTANCE THERMOMETRY AT LOW TEMPERATURES1, Journal of the American Chemical Society, 47, 326–332, doi:10.1021/ja01679a007, https://doi.org/10.1021%2Fja01679a007, 1925.

Huber Kältemaschinenbau AG: 77656 Offenburg, Germany, http://www.huber-online.com/en/.

Incropera, F. P. and DeWitt, D. P.: Introduction to Heat Transfer, 5th ed., Wiley, Hoboken, N.J., 2007.

Kirkby, J. et al.: Role of sulphuric acid, ammonia and galactic cosmic rays in atmospheric aerosol nucleation, Nature, 476, 429–433, 2011.

Kupc, A., Amorim, A., Curtius, J., Danielczok, A., Duplissy, J., Ehrhart, S., Walther, H., Ickes, L., Kirkby, J., Karten, A., Lima, J., Mathot, S., Minginette, P., Onnela, A., Rondo, L., and Wagner, P.: A fibre-optic UV system for H2SO4 production in aerosol chambers causing minimal thermal effects, Journal of Aerosol Science, 42, 532 – 543, doi:http://dx.doi.org/10.1016/j.jaerosci.2011.05.001, http://www.sciencedirect.com/science/article/pii/S0021850211000632, 2011.

Myhre, G., Shindell, D., Bréon, F., and Collins, W.: Anthropogenic and natural radiative forcing, Climate Change 2013: The Physical Science Basis (eds. Stocker, T.F., et al.), pp. 571–658, 2013.

National Instruments Corp.: Berkshire RG14 2PZ, United Kingdom, http://www.ni.com/en-gb.html.

Opsens Inc.: Quebec, Canada, https://opsens.com.

Voigtlander, J., Duplissy, J., Rondo, L., Kurten, A., and Stratmann, F.: Numerical simulations of mixing conditions and aerosol dynamics in the CERN CLOUD chamber, Atmospheric Chemistry and Physics, 12, 2205–2214, doi:10.5194/acp-12-2205-2012, http://www.atmos-chem-phys.net/12/2205/2012/, 2012.

WIKA Alexander Wiegand SE & Co. KG: 63911 Klingenberg, Germany, http://en-co.wika.de/home_en_co. WIKA.
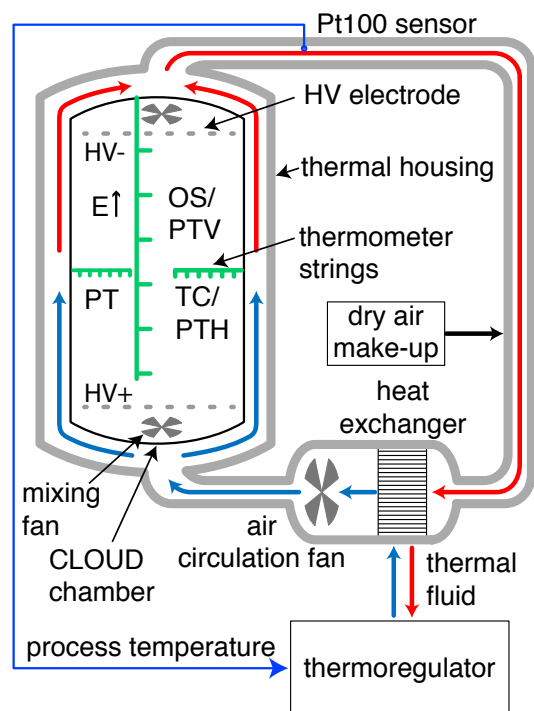
Figure 1. Schematic of the CLOUD thermal system. Thermally-controlled air is circulated by a fan at a rate of around 7200 m^3/h within a thermally-insulated housing surrounding the stainless steel CLOUD chamber (3 m diameter, 26.1 m^3 volume). The air is returned to the bottom of the chamber along an insulated duct, where it passes through a heat exchanger. A small flow of dessicated air is added to compensate for leaks and ensure that the dew point of the re-circulated air remains well below -80°C. The air is precisely maintained at a selectable "process temperature" in the range between -70°C and +100°C by a 36 kW thermoregulator (Unistat 850W; Huber Kältemaschinenbau AG) which controls the temperature of thermal fluid circulating through the heat exchanger. Fresh make-up air and trace gases continuously enter the chamber to compensate for sampling losses and maintain 5 mbar over-pressure inside the chamber. The chamber air is injected underneath the lower mixing fan at rates between 20 l/min (during calibration campaigns) and 210 l/min (during CLOUD data campaigns). During data campaigns, vertical electrical fields of up 20 kV/m are generated inside the CLOUD chamber by a pair of HV electrodes whose mid-plane (at 0 V potential) coincides with the mid plane of the chamber. The temperature of the air inside the CLOUD chamber is measured by several precision thermometer strings, indicated by green lines.
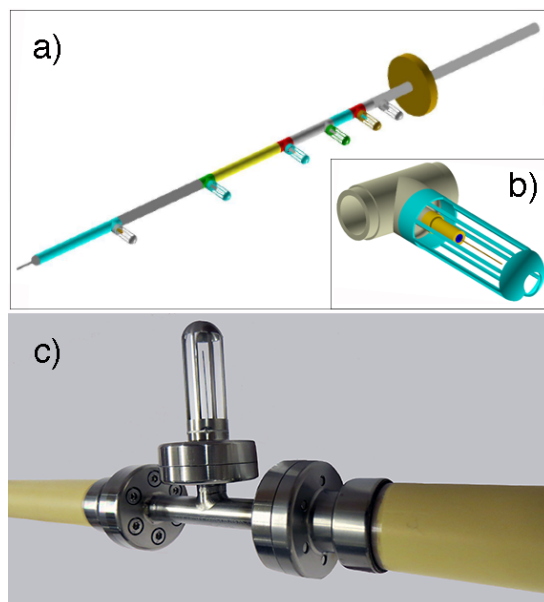
Figure 2. Images of two temperature strings showing a) a model drawing of the thermocouple (TC) string with 6 TC sensors and one Pt100 sensor at the tip, mounted on a 1.25 m stainless steel support tube welded to a DN100 flange, b) a model drawing of a single TC sensor (thin brown line), and c) a photograph of an approximately 25 cm section of the optical sensor string showing a sensor mounted inside a stainless steel capillary and transition structure that is welded to two partially-conducting zirconia ceramic tube spacers of 27 mm outer diameter (yellow). The sensors are mounted inside Faraday cages (e.g. coloured blue in panel b) to protect against corona discharge when a 20 kV/cm vertical electric field is present in the CLOUD chamber. Ultra-clean materials (stainless steel and ceramics) are used throughout, with the readout wires/optical fibres passing inside the hollow support structures.

Table 1. Position of the temperature sensors in CLOUD. The CLOUD chamber is a cylinder of 150 cm radius (r) and approximately 400 cm height (z). The origin of the cylindrical coordinate system is located in the centre of the chamber, with the z axis pointing vertically upwards. The Pt100 calibration strings, PTH and PTV, have sensor locations that closely match those of the TC and OS strings, respectively. The calibration strings, which are only installed during calibration measurements, are displaced laterally from the TC string by Δz = -20 cm (PTH) and from the OS string by 10 cm azimuthally (PTV).

Sensor #	Horizontal thermocouple string (TC) and Horizontal Pt100 calibration string (PTH)		Vertical optical string (OS) and Vertical Pt100 calibration string (PTV)		Horizontal Pt100 string (PT)	
	Radius, r (cm)	Height, z (cm)	Radius, r (cm)	Height, z (cm)	Radius, r (cm)	Height, z (cm)
1	145	0	50	123.1	145	0
2	138	0	50	78.3	115	0
3	128	0	50	33.5	90	0
4	115	0	50	-11.3	-	-
5	90	0	50	-56.1	60	0
6	60	0	50	-100.9	-	-
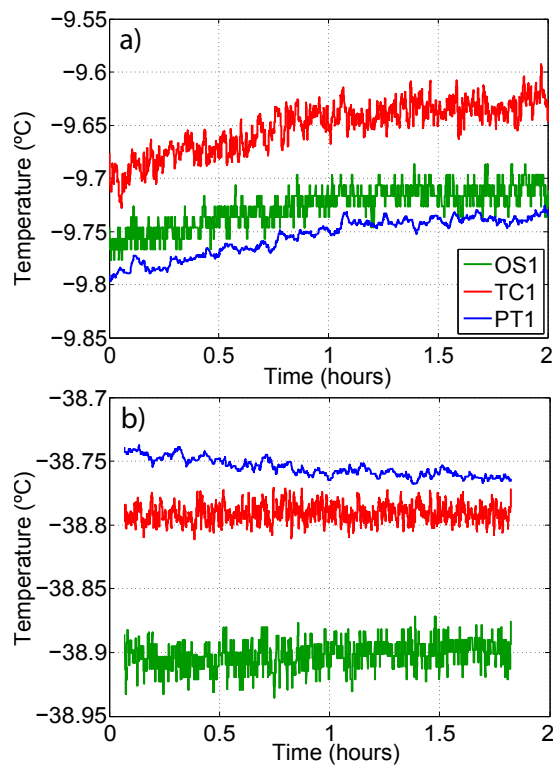
Figure 3. Examples of the typical temperature stability in the CLOUD chamber over a period of several hours: a) during an experimental data run and b) during a calibration run (OS, optical sensor; TC, thermocouple, TC; and PT, Pt100 sensor). The temperature drift in panel a) can result from setting new experimental conditions such as the addition of ultra violet radiation or trace gases, which causes a slight change in equilibrium temperature. The measurements are smoothed with a 15 s median window.
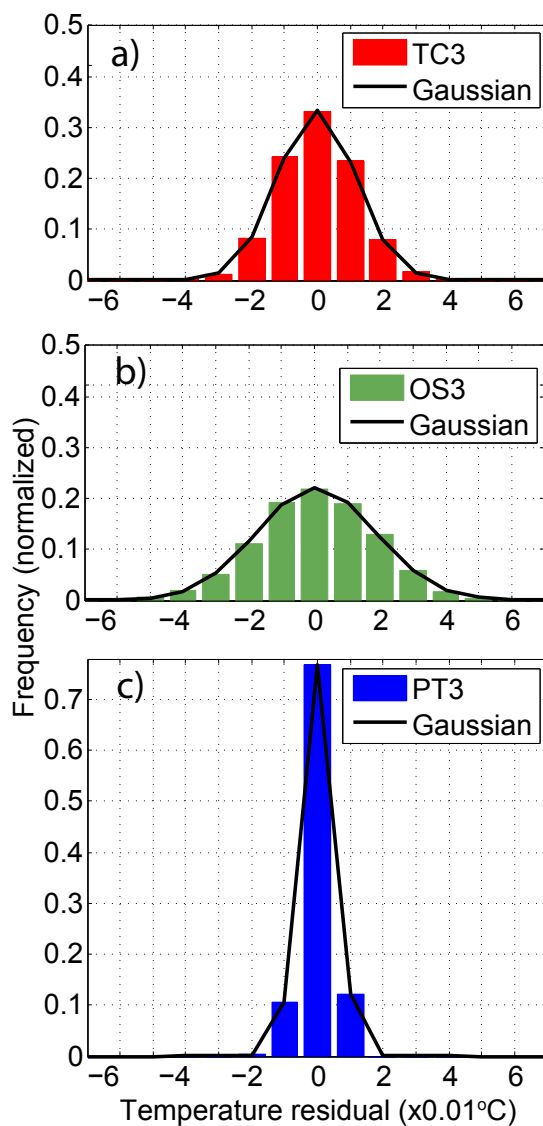
Figure 4. Temperature residuals from their mean values over periods of several hours during calibration runs for a) TC3 at -40°C, b) OS3 at -0°C and c) PT3 at -30°C. The measurements are smoothed with a 15 s median window, and slow trends in the data have been removed. The standard deviations of Gaussian fits to the data are a) 0.012°C, b) 0.018°C, and c) 0.004°C.
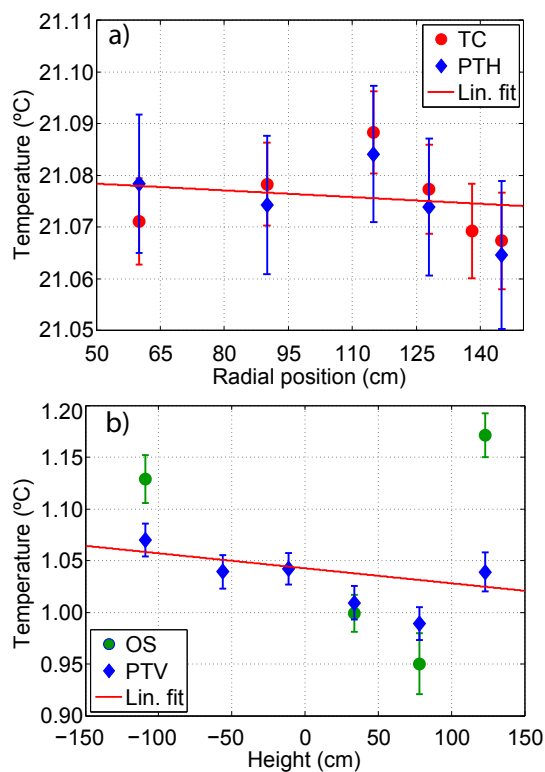
Figure 5. Comparison of the temperature non-uniformity measured by several sensor strings in a) the radial and b) the vertical directions during calibration runs at 21°C and 1°C, respectively. Linear fits are shown to guide the eye. OS4 and OS5 are not included in panel b (see Appendix A for details). The error bars in this and other figures show 1 sigma statistical uncertainties and do not account for possible systematic uncertainties.
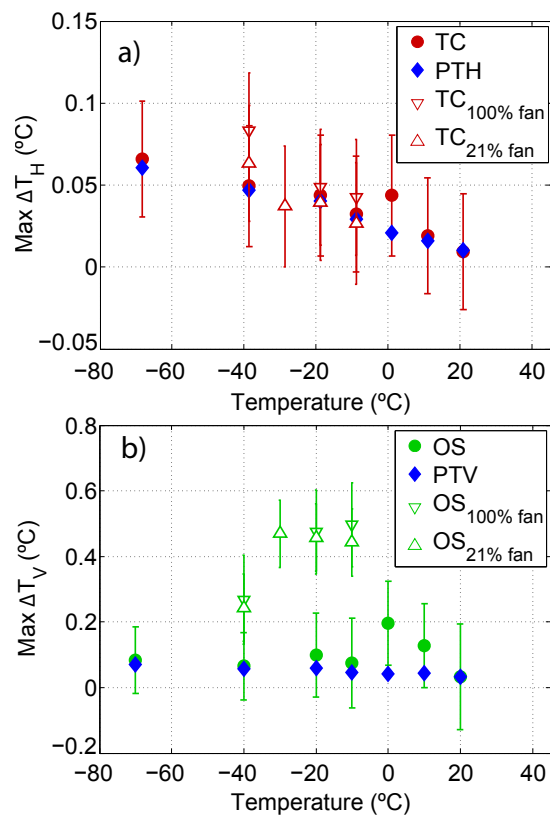
Figure 6. Maximum temperature difference from the string mean (temperature non-uniformity), ΔT, in the a) horizontal and b) vertical directions at chamber temperatures between -70°C and 20°C. The data were recorded during both calibration and data-taking runs in June and November 2014, respectively.
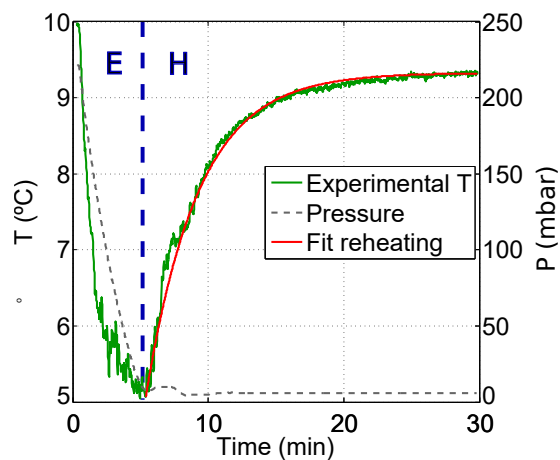
Figure 7. Example of an adiabatic pressure reduction to form a cloud in the CLOUD chamber. The chamber pressure is reduced from 220 mbar to 5 mbar above one atmosphere pressure during a period of 5 minutes (dashed curve and right-hand scale). This produces of reduction of the air temperature by around 5°C (green curve and left-hand scale, recorded by a TC sensor). Provided the initial relative humidity is sufficiently high, a liquid cloud forms in the chamber during the cool period. The air in the chamber then returns to its equilibrium temperature set by the relatively warm chamber walls, and the cloud eventually evaporates. In this example the initial air temperature, before expansion, had not yet reached the equilibrium value near 9.3°C. The red line is an exponential fit to the warming period with a time constant of 200 s (Eq. 1).
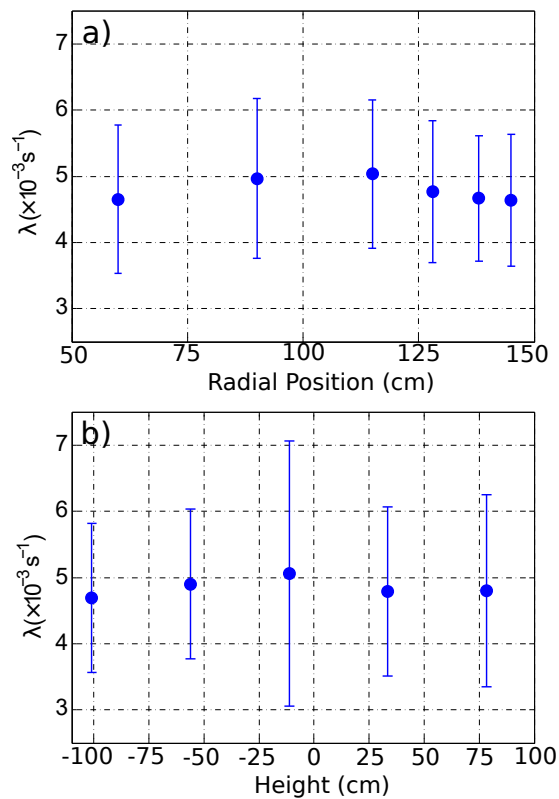
Figure 8. Air reheating rates (λ) following an adiabatic pressure reduction versus a) radial and b) vertical position in the chamber.
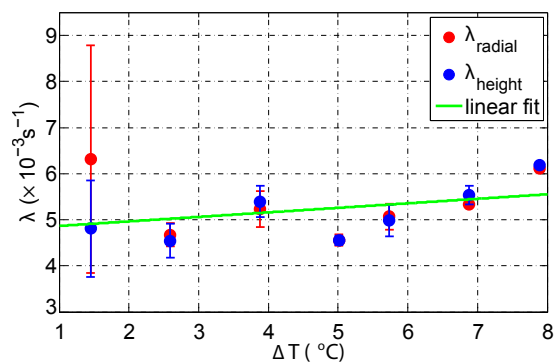
Figure 9. Air reheating rates (λ) following an adiabatic pressure reduction versus the initial temperature reduction.
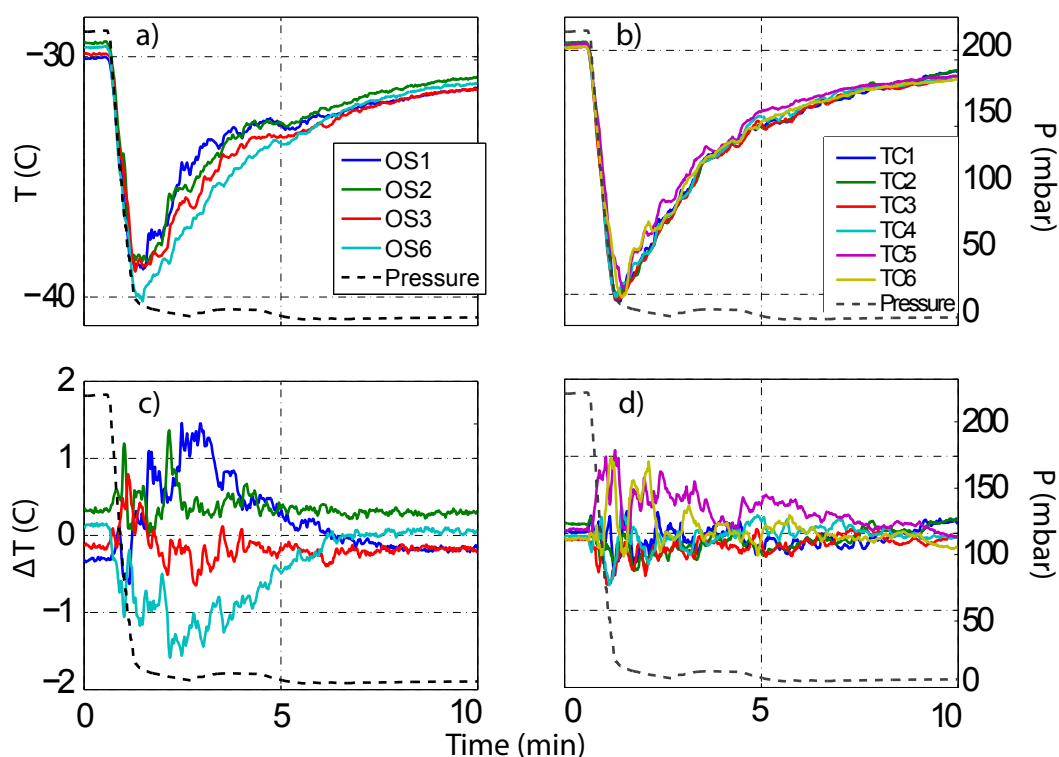
Figure 10. Temperature non-uniformities following an adiabatic pressure reduction during CLOUD9 at -30°C in a) the vertical direction (OS) and b) the horizontal direction (TC). Panels c and d show the residuals from the mean temperatures in the vertical and horizontal directions, respectively. The relative air pressures are shown by dashed curves. Compared with operation under equilibrium conditions (Fig. 6), larger non-uniformities of up to around ±1.0°C are present at the minimum temperature during adiabatic pressure reductions.
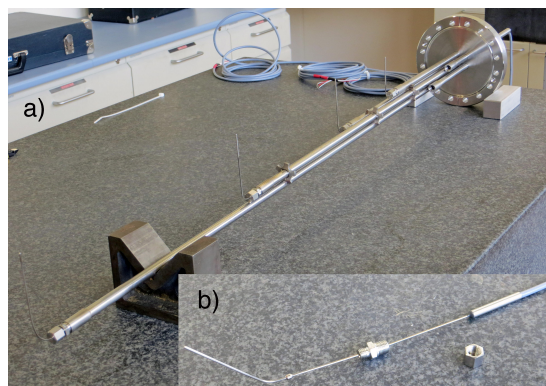
Figure A1. The horizontal Pt100 calibration string (PTH) showing a) the string during assembly, with 4 of the 6 sensors mounted and b) a single Pt100 sensor before mounting in the string (a 1.5 mm diameter stainless steel sheath surrounds the actual Pt100 sensor). The Pt100 calibration strings are designed to allow the sensors to be dismounted without disconnecting from their readout electronics.
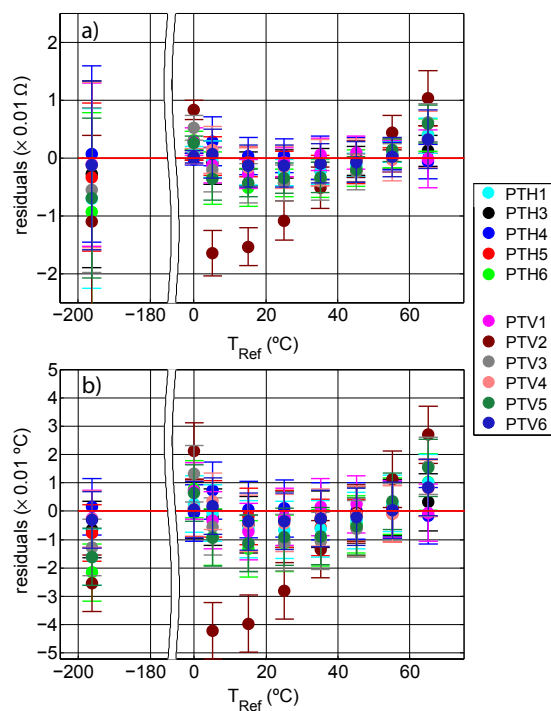
Figure A2. Residuals of the least squares fits to the CVD equation (Eq. A1 and Table A1), for the horizontal (PTH) and vertical (PTV) Pt100 calibration strings versus temperature: a) resistance residuals and b) temperature residuals. The data were obtained during the laboratory calibration, July 2014.

Table A1. Fitted parameters and one standard deviation uncertainties of the Callendar-van-Dusen (CVD) coefficients (Eq. A1) for the horizontal and vertical Pt100 calibration strings, PTH and PTV, obtained during the laboratory calibration, July 2014. The parameter C was fixed at $-4.183 \times 10^{-12}\ \Omega\ °C^{-3}$.

	R_0^{fit}	σR_0	A^{fit}	σA	B^{fit}	σB	Fit R^2
PTH1	100.0322	9.36E-4	3.908E-3	3.25E-07	-6.62E-07	3.70E-09	0.9991
PTH3	100.0216	2.55E-4	3.908E-3	1.27E-07	-6.70E-07	1.55E-09	0.9998
PTH4	99.98723	3.06E-4	3.914E-3	1.03E-07	-6.54E-07	1.06E-09	0.9999
PTH5	100.0453	6.86E-4	3.907E-3	2.26E-07	-6.60E-07	2.35E-09	0.9995
PTH6	100.0182	1.98E-3	3.913E-3	5.80E-07	-6.46E-07	5.80E-09	0.9982
PTV1	100.0496	1.11E-3	3.910E-3	3.17E-07	-6.61E-07	2.52E-09	0.9996
PTV2	100.0364	5.26E-3	3.908E-3	1.59E-06	-6.87E-07	1.35E-08	0.9894
PTV3	100.0503	2.61E-3	3.909E-3	6.64E-07	-6.69E-07	5.46E-09	0.9981
PTV4	100.0355	5.17E-4	3.912E-3	1.81E-07	-6.49E-07	1.52E-09	0.9999
PTV5	100.0184	1.79E-3	3.910E-3	5.32E-07	-6.80E-07	5.19E-09	0.9979
PTV6	100.0108	3.91E-4	3.912E-3	1.51E-07	-6.48E-07	1.37E-09	0.9999
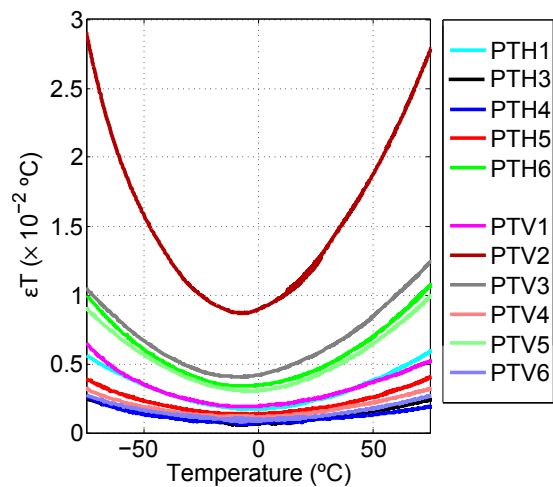
Figure A3. Estimated uncertainty of the temperature measurement of each Pt100 calibration sensor versus temperature, based on the individual fits of the laboratory calibration measurements to the CVD equation. After calibration, almost all sensors have an uncertainty below 0.01°C over the indicated temperature range.
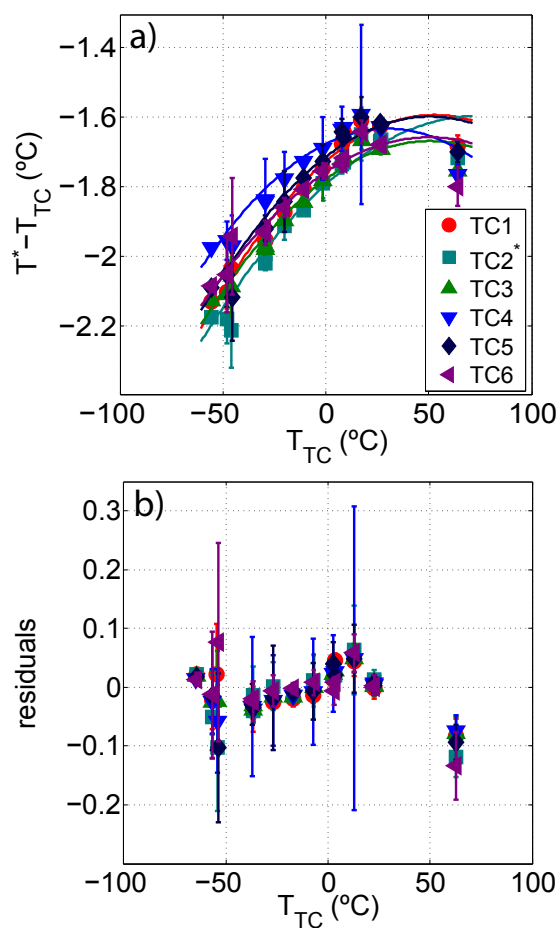
Figure A4. Calibration of the TC string during during the CLOUD calibration campaign: a) fitted calibration curves (Eq. A2 with $k_s = 2$) and b) residuals from the calibration fit. There was a malfunction of the Pt100 sensor (PTH2) for TC2 so the PTH2 values were obtained by interpolation between PTH1 and PTH3.

Table A2. Fitted calibration parameters and one standard deviation uncertainties for the thermocouple string obtained during the CLOUD calibration campaign.

Sensor	x_2	σx_2	x_1	σx_1	x_0	σx_0	χ^2/ν
TC1	-6.39E-5	1.28E-5	4.47E-2	4.40E-04	-1.70	1.50E-02	0.34
TC2	-6.04E-5	1.36E-5	4.27E-2	7.74E-04	-1.74	1.70E-02	0.44
TC3	-6.17E-5	1.01E-5	3.85E-2	3.46E-04	-1.75	1.20E-02	0.25
TC4	-6.39E-5	1.56E-5	2.35E-2	1.10E-03	-1.66	1.80E-02	0.71
TC5	-6.55E-5	2.17E-5	4.01E-2	7.23E-04	-1.68	2.50E-02	1.41
TC6	-6.51E-5	1.31E-5	2.93E-2	4.45E-04	-1.72	1.60E-02	0.46
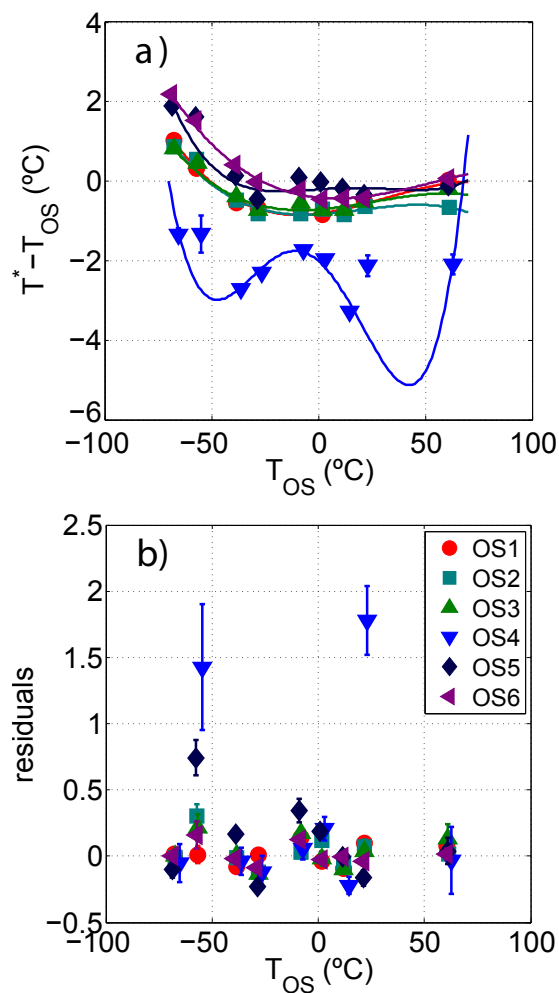
Figure A5. Calibration of the OS string during during the CLOUD calibration campaign: a) fitted calibration curves (Eq. A2 with $k_s = 3$ or 4) and b) residuals from the calibration fit.

Table A3. Fitted calibration parameters and one standard deviation uncertainties for the optical sensor string obtained during the calibration campaign.

Sensor	x_4	σx_4	x_3	σx_3	x_2	σx_2	x_1	σx_1	x_0	σx_0	χ^2/ν
OS1	N/A	N/A	-3.81E-6	2.93E-6	2.68E-4	1.48E-4	9.60E-3	9.30E-3	-7.42E-1	2.01E-1	28.40
OS2	N/A	N/A	-4.35E-6	1.97E-6	1.75E-4	8.66E-5	7.34E-3	6.60E-3	-7.65E-1	1.33E-1	7.02
OS3	N/A	N/A	-2.89E-6	2.23E-6	2.30E-4	1.04E-4	5.74E-3	7.10E-3	-7.22E-1	1.86E-1	12.34
OS4	2.54E-7	2.52E-7	-1.01E-6	8.71E-6	-1.04E-3	1.00E-3	1.12E-3	2.76E-2	-1.74	0.46	4.67
OS5	1.36E-7	3.48E-7	-1.09E-6	1.23E-5	3.77E-4	1.50E-3	5.27E-3	3.89E-2	-3.25E-2	6.97E-1	45.72
OS6	N/A	N/A	-2.16E-6	2.66E-6	3.27E-4	1.27E-4	4.64E-3	7.50E-3	-408E-1	1.74E-1	19.32

Table A4. Fitted calibration parameters and one standard deviation uncertainties for the Pt100 string during the calibration campaign.

	x_0	σx_0	x_1	σx_1	Fit R^2
PT1	0.561	0.020	1.011	0.001	1.00
PT2	0.187	0.083	1.012	0.002	1.00
PT3	0.453	0.020	1.007	0.001	1.00
PT5	0.335	0.025	0.998	0.001	1.00